UC Santa Cruz
UC Santa Cruz Previously Published Works

Title

Decomposing electronic and lattice contributions in optical pump – X-ray probe transient inner-shell absorption spectroscopy of CuO

Authors

Mahl, Johannes
Neppl, Stefan
Roth, Friedrich
et al.

Peer reviewed

Ultrafast Photoinduced Energy and Charge Transfer

ARTICLE

Decomposing Electronic and Lattice Contributions in Optical Pump–X-ray Probe Transient Inner-Shell Absorption Spectroscopy of CuO

Johannes Mahl[a,b], Stefan Neppl[a,c], Friedrich Roth[d,e], Mario Borgwardt[a], Catherine Saladrigas[a,f], Benjamin Toulson[a], Jason Cooper[g], Tahiyat Rahman[a], Hendrik Bluhm[a,h], Jinghua Guo[h], Wanli Yang[h], Nils Huse[b,e], Wolfgang Eberhardt[e,h], and Oliver Gessner[a]

Electronic and lattice contributions to picosecond time-resolved X-ray absorption spectra (trXAS) of CuO at the oxygen K-edge are analyzed by comparing trXAS spectra recorded with excitation wavelengths of 355 nm and 532 nm with quasi-static, temperature-dependent XAS measurements. Laser-induced changes are largely reproduced by heating-induced XAS modifications, indicating that the trXAS spectra at pump-probe time-delays ≥150 ps are dominated by lattice heating effects. In particular, for the 532 nm experiment at ~5 mJ/cm^2 fluence, both the initial sample temperature and its dynamic evolution are well captured by a one-dimensional thermal energy deposition and diffusion model. The thermal conductivity $k = (1.3\pm0.4)$ Wm^{-1}K^{-1} derived from this model is in good agreement with the literature value for CuO powder $k_{powder} = 1.013$ Wm^{-1}K^{-1} and approximately an order of magnitude smaller than the smallest literature value $k_{bulk} = 18$ Wm^{-1}K^{-1} for bulk CuO. The findings are rationalized by surface morphology changes during the sample preparation by thermal oxidation of Cu, as previously observed by atomic force microscopy (AFM). For 355 nm excitation, a quantitative analysis of the experiments is hampered by the large temperature gradients within the probed sample volume owing to the small UV penetration depth. Large discrepancies between estimated and measured temperatures in the 355 nm experiment are tentatively assigned to the more challenging modelling conditions and, potentially, the existence of radiative relaxation pathways.

a. Chemical Sciences Division, Lawrence Berkeley National Laboratory, Berkeley, CA, USA
b. Physics Department Universität Hamburg, Hamburg, Germany
c. Helmholtz-Zentrum Berlin für Materialien und Energie, Berlin, Germany
d. Institute for Experimental Physics, TU Bergakademie Freiberg, Germany
e. Center for Free-Electron Laser Science DESY, Hamburg, Germany
f. Chemistry Department UC Berkeley, Berkeley CA, USA
g. Joint Center for Artificial Photosynthesis (JCAP), Berkeley, CA, USA
h. Advanced Light Source, Lawrence Berkeley National Laboratory, Berkeley, CA, USA

1. Introduction

As research in the field of ultrafast X-ray science progresses toward the use of high repetition rate X-ray free-electron lasers[1,2] and high-order harmonic generation (HHG) light sources,[3,4] it is crucial to understand the impact of corresponding high-repetition rate excitation processes on non-replenishing samples that are typical for many applications in materials and chemical sciences. Thermal excitations and their X-ray spectroscopic fingerprints play a particularly important role as they are a ubiquitous, mostly unintended consequence of virtually all photon absorption processes in condensed phase materials through coupling of electronic and nuclear motion. Understanding and, in many cases, mitigating the impact of thermal excitations on ultrafast X-ray spectroscopy and scattering signals is crucial for the success of a large range of experiments. This applies, in particular, to dynamics that are strongly coupled to thermal excitations[5] and/or that extend beyond the first ~100 fs after photoexcitation where signal contributions from lattice motion due to electron-phonon coupling may become relevant.[6] Despite their importance, systematic studies of the relative contributions and dynamic trends of electronic and lattice excitations in time-resolved X-ray spectroscopy data are scarce to date. Hayes et al. found that photoinduced changes in the iron K-edge X-ray absorption spectrum of hematite (α-Fe_2O_3), recorded 100 ps after super-bandgap excitation with 3.5 eV photons, are entirely dominated by lattice heating effects.[7] Lin et al. used femtosecond time-resolved XUV absorption spectroscopy to investigate photoinduced dynamics in PbI_2.[8] The transient XUV spectra in this study are well reproduced by lattice temperature dependent changes for pump-probe delays greater than ~4 ps. In an attosecond time-resolved XUV transient absorption experiment on silicon, Schultze et al. observed lattice-motion induced band-gap modifications as early as ~60 fs after photoexcitation.[6] Evidently, signal contributions due to lattice motion are an integral part of time-resolved X-ray spectroscopy that can have decisive impact on the feasibility of experiments. It is essential, to characterize these contributions and to understand their dynamics based on the underlying physics.

Here, we study photoinduced dynamics in the transition metal oxide semiconductor CuO (cupric oxide) using picosecond time-resolved laser-pump/X-ray-probe transient absorption spectroscopy (trXAS). CuO is a p-type semiconductor with possible applications in photocatalytic degradation of organic pollutants,[9,10] hydrogen production from water,[11-13] and as anode material in lithium batteries.[14] In many of these applications, CuO is used in conjunction with wide gap semiconductors, such as ZnO and TiO_2, to cover a large portion of the solar spectrum. In the experiments presented here, a CuO film is studied that is generated by thermal surface oxidation of a sheet of copper. The trXAS experiments are performed at the oxygen K-edge near ~540 eV using a previously described optical-pump/X-ray-probe picosecond trXAS setup at beamline 8 of the Advanced Light Source (ALS).[15] The pump pulse repetition rate of 127 kHz is comparable to the current 100 kHz design target for the first stage of the Linac Coherent Light Source upgrade (LCLS II). Pump-probe experiments are performed at two different photon energies of 2.33 eV and 3.49 eV and complemented by quasi-static, temperature-dependent XAS measurements in order to explore the relative contributions of electronic and lattice dynamics to the trXAS spectra. Band gap values for CuO have been reported across a range of ≈1.0-2.1 eV,[16-23] thus, both laser wavelengths induce super-bandgap excitations. Relaxation to the conduction band minimum via electron-phonon coupling occurs on timescales much smaller than the 70 ps time resolution of the experiment. Therefore, the main difference between measurements with the two different wavelengths is the transfer of an additional 1.2 eV into phonons before relaxation across the band gap, i.e., a potentially higher lattice temperature after excitation with 355 nm, assuming the same number of excitations per unit sample volume. Thus, comparing measurements for both excitation wavelengths with the same excitation density and with the same total excitation energy (photon energy × excitation density) provides insight into the relative impact of electronic and lattice contributions to the trXAS spectra.

Relaxation dynamics are monitored across a pump-probe time-delay range of ~350 ns. The

ARTICLE

photoinduced trXAS dynamics are compared to purely temperature-induced effects, acquired by recording quasi-static XAS spectra with the sample heated to temperatures between 53˚C and 145˚C. The photoinduced changes in the CuO oxygen K-edge trXAS spectra recorded ≥150 ps after photoexcitation with either 355 nm or 532 nm are well reproduced by effects due to increased lattice temperatures. The steady-state temperature-dependent XAS measurements are used to create a "temperature ruler" for the trXAS data, yielding picosecond-time resolved lattice temperature trends. Temperatures for both excitation wavelengths at comparable pump laser fluences of ~5 mJ/cm^2 exhibit initially fast relaxation dynamics that slow down on a tens of nanoseconds timescale and can be described by bi-exponential decay with time constants of ~10 ns and ~300 ns. These dynamics are well reproduced by a one-dimensional thermal diffusion model that explicitly takes into account the depth-dependent intensity distributions of both the UV/vis pump pulses as well as the X-ray probe pulse. Comparison of the 355 nm and 532 nm results illustrates that a detailed modeling of these depth-dependent intensity profiles is crucial for a quantitative understanding of the physics underlying the laser-induced heating and subsequent cooling processes and their impact on the recorded trXAS spectra. The measurements yield a thermal conductivity of the CuO film of k = (1.3±0.4) Wm^{-1}K^{-1}, which is in good agreement with the literature value for CuO powder (1.013 Wm^{-1}K^{-1})[24] and approximately an order of magnitude smaller than the smallest literature value for bulk CuO (18 Wm^{-1}K^{-1})[25]. The findings are rationalized by surface morphology modifications during the sample preparation by thermal annealing, which have previously been documented by temperature-dependent atomic force microscopy (AFM).[26]

2. Experimental details

2.1 Sample preparation Copper sheet metal is cut to size and the surface roughened with sand paper to create better adhesion of the CuO film grown on the Cu substrate. This is followed by cleaning with micro-soap, acetone and ethanol in this

order. The samples are then transferred to a furnace and heated to 500°C for 15 minutes in normal atmosphere. During this procedure, the sample surface oxidizes, creating a layer of CuO.[26-28] After cooling, the sample is gently wiped with an ethanol-soaked lint-free tissue. The heating-cooling-wiping cycle is repeated a total of five times. While the exact value for the final CuO film thickness is unknown, it is large compared to the ~43 nm probing depth of the X-rays (see section 2.3), since no significant count rate fluctuation is observed while raster-scanning the sample. Fig. 1a shows static X-ray absorption spectra acquired in total electron yield (TEY, blue) and total fluorescence yield (TFY, black) mode at beamline 8.0.1.2 of the Advanced Light Source (ALS). The spectra agree well with TEY measurements by Jiang et al., shown in red.[29] For comparison, the Cu$_2$O spectrum by Jiang et al. is also included (gray, dashed). The absence of the main Cu$_2$O resonance feature at 532.5 eV indicates a high purity of the prepared CuO film. The slightly better agreement, concerning the amplitude, between the TEY spectra compared to the TFY spectrum is likely due to saturation effects in the TFY signal.[30] The latter are minimized by choosing a geometry with a normal X-ray incidence angle and grazing angle X-ray fluorescence detection (≈0° and ~80°, respectively, relative to the sample surface normal). Fig. 1b shows static TFY spectra from all samples used for time-resolved measurements presented here, demonstrating very good reproducibility of the sample preparation and experimental conditions. All spectra are normalized to the same increase of 0 to 1 between pre- and post-edge signals.

2.2 Time-resolved XAS For the trXAS experiment, a mobile laser pump - X-ray probe setup is employed at beamline 8.0.1.2 of the ALS. The setup and its operation have previously been described in detail.[15] Briefly, CuO samples are with carbon tape attached along horizontal and vertical directions providing a straight edge. The laser pointing is adjusted with a piezo-actuator controlled mirror mount to coincide with the X-rays. The X-ray and laser focus spot sizes are
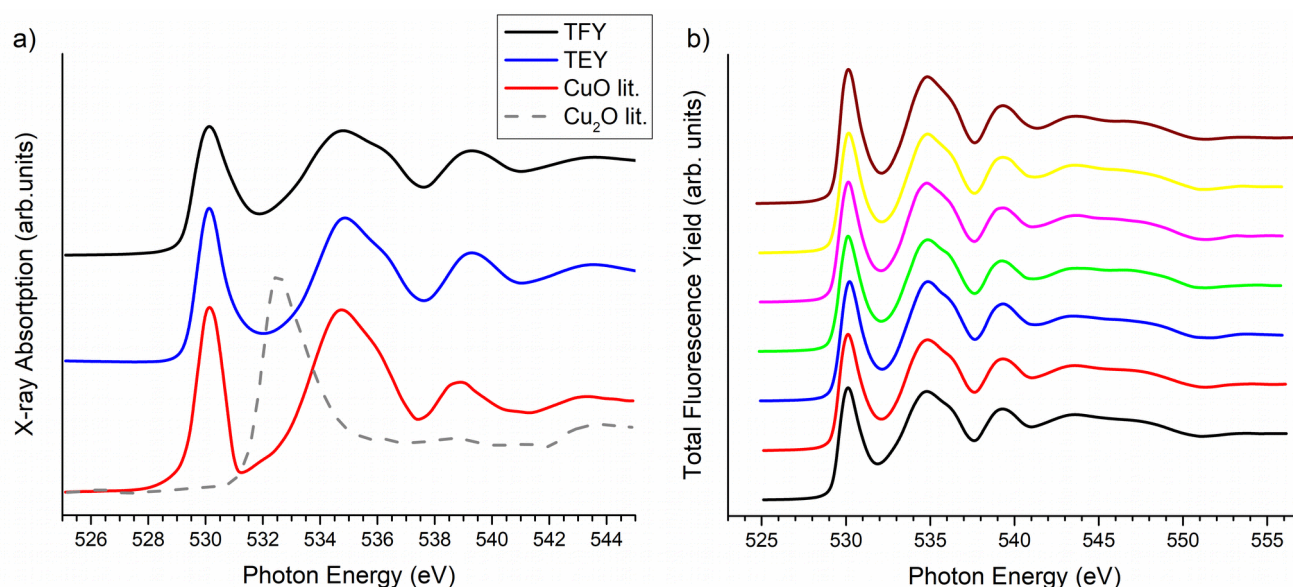

Fig. 1. (a) Comparison of static oxygen K-edge XAS spectra of CuO acquired TEY (blue) and TFY (black) mode with CuO and Cu$_2$O reference spectra from Jiang et al.[29] (b) Static TFY spectra from all samples used for time-resolved measurements. Spectra in a) and b) have been offset vertically for improved clarity.

excited with 10 ps full-width-at-half-maximum (FWHM) laser pulses of either 532 nm (2.33 eV) or 355 nm (3.49 eV) wavelength (photon energy) and interrogated with 70 ps long X-ray pulses from the ALS. Time-dependent oxygen K-edge absorption spectra are recorded in total fluorescence yield (TFY) mode with a time-sensitive micro-channel plate detector.[31] The detector is capable of distinguishing TFY signals from individual ALS pulses, enabling the simultaneous recording of trXAS spectra at multiple laser-pump/X-ray-probe time delays. The laser system is synchronized to the ALS and operated at ~127 kHz repetition rate. A comparison of trXAS spectra recorded at negative time delays with XAS spectra recorded with the laser beam blocked, shows that the sample has fully relaxed between successive pump pulses.

Inside the vacuum system, the pump and probe beams are combined by reflecting the laser beam off a mirror with a hole in the center that allows the X-rays to pass through. Spatial pump-probe overlap is achieved by performing knife-edge scans for both beams using a photodiode

180 × 80 µm^2 and ~250 × 200 µm^2 (horizontal × vertical, FWHM), respectively, ensuring that the probed sample area was homogeneously excited. Larger laser spot sizes would unnecessarily increase the total deposited energy (mJ) per shot at a given excitation fluence (mJ/cm^2), leading to additional sample heating and, potentially, damage. The laser spot sizes were approximately the same for both laser colors. Temporal pump-probe overlap is adjusted using a biased photodiode with 30 ps response time and a digital oscilloscope with 1 GHz bandwidth and 10 GS/s sample rate.

The ALS was operated in multi-bunch mode with 2 ns bunch-to-bunch spacing. Thus, individual TFY spectra have pump-probe delays of $\Delta t_N = t_N - t_0 = \Delta t_0 + 2$ ns $* (N-1)$, where Δt_0 is the pump-probe delay of the first X-ray pulse after the laser pulse and N = 1,2,3,... indicates the Nth X-ray pulse following the laser pulse. The minimum pump-probe delay is set to $\Delta t_0 = (150 \pm 30)$ ps for all measurements presented here. The simultaneous recording of trXAS spectra from an extended X-ray pulse train enables the capture of dynamics across hundreds of nanoseconds,

while for delays <2 ns, the pump-probe delay Δt_0 can be varied by a programmable, electronic delay line. Excited state spectra ("pumped") are compared to ground state reference spectra ("unpumped") by creating difference spectra ΔtrXAS for each pump-probe delay (ΔtrXAS(Δt) = trXAS(pumped, Δt) – trXAS(unpumped)). Any given pumped spectrum is compared to an unpumped spectrum stemming from the same ALS electron bunch, but acquired one round-trip (656 ns) before laser excitation. This procedure ensures minimum impact of bunch-to-bunch variations in the ALS fill pattern on the ΔtrXAS spectra. Long-term variations of the bunch fill pattern are accounted for using bunch current monitor data supplied by the ALS. Additionally, photon energy dependent variations of the average incident X-ray flux are monitored via a gold mesh placed in the X-ray beam downstream from the last beamline optic.

The sample is raster-scanned with 250 μm/s scan speed and a 500 μm spacing between neighboring lines. The main reason for this procedure is to avoid thermally induced conversion of CuO to Cu_2O, which is particularly noticeable when pumping with 355 nm pulses. High temperatures in conjunction with low partial pressures of oxygen lead to a CuO to Cu_2O phase transition.[32][33] The effect is more pronounced in the 355 nm measurement, most likely due to the smaller penetration depth of 355 nm light compared to 532 nm photons,[34] which leads to higher transient surface temperatures under UV exposure (see section 4). The scan speed is chosen such that upon recording of an XAS spectrum on an already laser-scanned sample area, no contributions from the intense Cu_2O white line at 532.5 eV (Fig. 1a) is detected. Note that the scanning procedure is essential to avoid artifacts due to overlapping transient features from CuO and Cu_2O.[15]

2.3 Selection of pump laser fluences Experiments are performed using pump laser photon energies (wavelengths) of 3.49 eV (λ=355 nm) and 2.33 eV (λ=532 nm), both of which are beyond the band gap of CuO ($\approx$1.0-2.1 eV[16-23]). For each laser wavelength, measurements are performed at two different fluences, 2.7 mJ/cm^2 and 4.6 mJ/cm^2 at 355 nm and 1.7 mJ/cm^2 and 4.8 mJ/cm^2 at 532 nm. Fluences are estimated based on

the assumption that the FWHM laser focus area contains $\approx$50% of the pulse energy. The two higher fluence values are chosen such that both the same fluence and the same total energy is deposited in the sample at each laser wavelength (with the laser spot sizes approximately the same for both colors). The 2.7 mJ/cm^2 fluence at 355 nm is chosen such that the average laser excitation density within the probed volume is expected to be comparable to that at 532 nm and 4.8 mJ/cm^2. This estimate takes into account the wavelength dependent reflectivities (11.3% and 9.9%, measured independently) and absorbances (1/e penetration depths 21.2 nm and 124.5 nm[28,34]) of the 355 nm and 532 nm pump pulses, respectively, as well as the X-ray penetration and escape depths at the angles of incidence (0˚) and detection ($\approx$80˚). The 1/e X-ray penetration depth undergoes significant changes around the absorption edge from 320 nm below (<528 eV) to 180 nm above (>543 eV) the edge.[35] For simplicity, the latter value (180 nm) is used as the average penetration depth for the incoming X-rays while the former (320 nm) is used for the 1/e escape depth of the X-ray fluorescence. Multiplying the two exponential decay functions that describe the X-rays entering and escaping the CuO sample and including the entrance and detection angles, leads to an effective 1/e X-ray probing depth of 43 nm. According to this estimate, the excitation densities within the probed volume for 355 nm and 532 nm pump pulses are comparable for a pump fluence ratio F_{532nm}/F_{355nm}= 1.73, which is very close to the experimental ratio 4.8 mJ/cm^2 / 2.7 mJ/cm^2 = 1.78. The measurement with 1.7 mJ/cm^2 fluence at 532 nm pump wavelength has been performed as an additional reference point to gauge the impact of the laser fluence on the response of the sample.

2.4 Temperature-resolved XAS The trXAS results are complemented by temperature-dependent, quasi-static X-ray absorption spectra (XAS_{temp}) recorded at ALS beamline 11.0.2. Temperature-dependent XAS_{temp} spectra are recorded in TFY mode using a photodiode covered with an Al filter suppressing background signal from ambient light. The sample is mounted on a button heater stage to control the sample temperature which is monitored with a

thermocouple on the front side of the sample. All measurements are performed at a 3 mTorr of oxygen background in order to increase the temperature at which the phase transition of CuO to Cu_2O starts to occur.[32][33] Temperature-induced difference spectra ΔXAS_{temp} are calculated by subtracting room temperature (RT) spectra from spectra acquired at elevated temperatures ($\Delta XAS_{temp}(\Delta T=T-RT) = XAS_{temp}(T)-XAS_{temp}(RT)$). For direct comparison of the $\Delta XAS_{temp}(\Delta T)$ and the $\Delta trXAS(\Delta t)$ spectra, the RT spectra were slightly corrected for an average sample warming effect induced by continued laser exposure (RT=28°C instead of 22°C, see section 4 for details).

3. Results

Fig. 2 illustrates the characteristic $\Delta trXAS$ effects of the CuO sample for various pump-probe time delays using the 355 nm, 4.6 mJ/cm^2 data set as

an example. Fig. 2a covers the full spectral range of the measurement, while Fig. 2b provides a magnified view in the range of the first resonance. The static XAS spectrum is overlaid in gray for reference. The left and right ordinate labels correspond to the XAS and $\Delta trXAS$ spectra, respectively. While the XAS units are arbitrary, they are the same for both the XAS and $\Delta trXAS$ spectra. The blue (0.15 ns) and green (2.15 ns) curves correspond to data from the first and second X-ray pulse after excitation, respectively. In order to investigate smaller differences at longer pump-probe delays, where the $\Delta trXAS$ signals are smaller, signals from multiple ALS bunches are averaged for this figure. The red curve (8.15 ns) is an average of three pulses (Δt=6.15-10.15 ns), the cyan curve (17.15 ns) of six pulses (Δt=12.15-22.15 ns) and the orange (180.15 ns) of 81 pulses (Δt=100.15-260.15 ns). For each of the averaged spectra, the indicated delay is the mean delay of the averaged spectra. The by far strongest effects are observed in the region of the first resonance at ≈530.1 eV (Cu
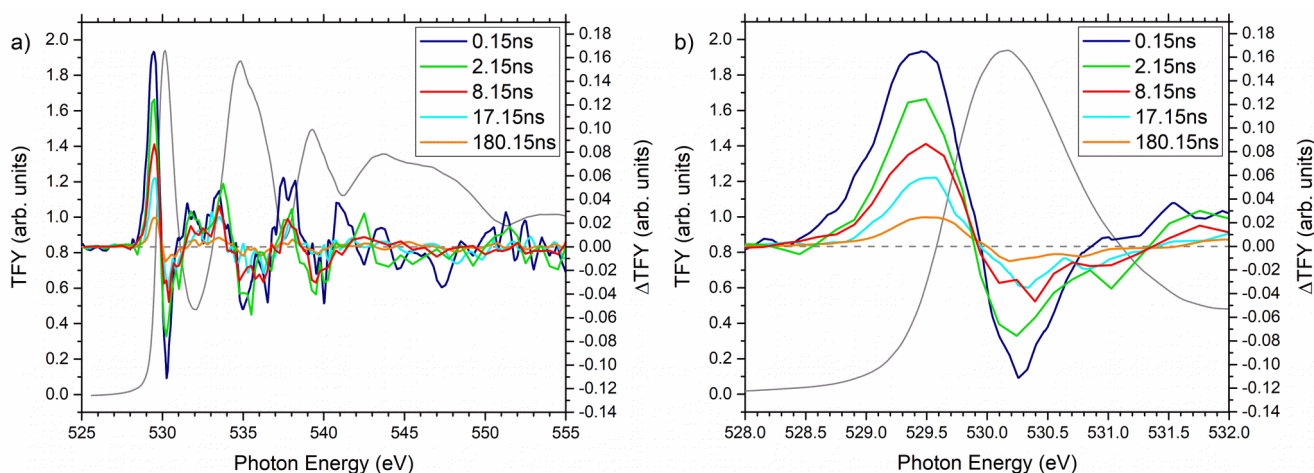

Fig. 2. a) Overview of the 355 nm 4.6 mJ/cm^2 trXAS data set. The reference spectrum (gray, left ordinate) is shown along with $\Delta trXAS$ spectra
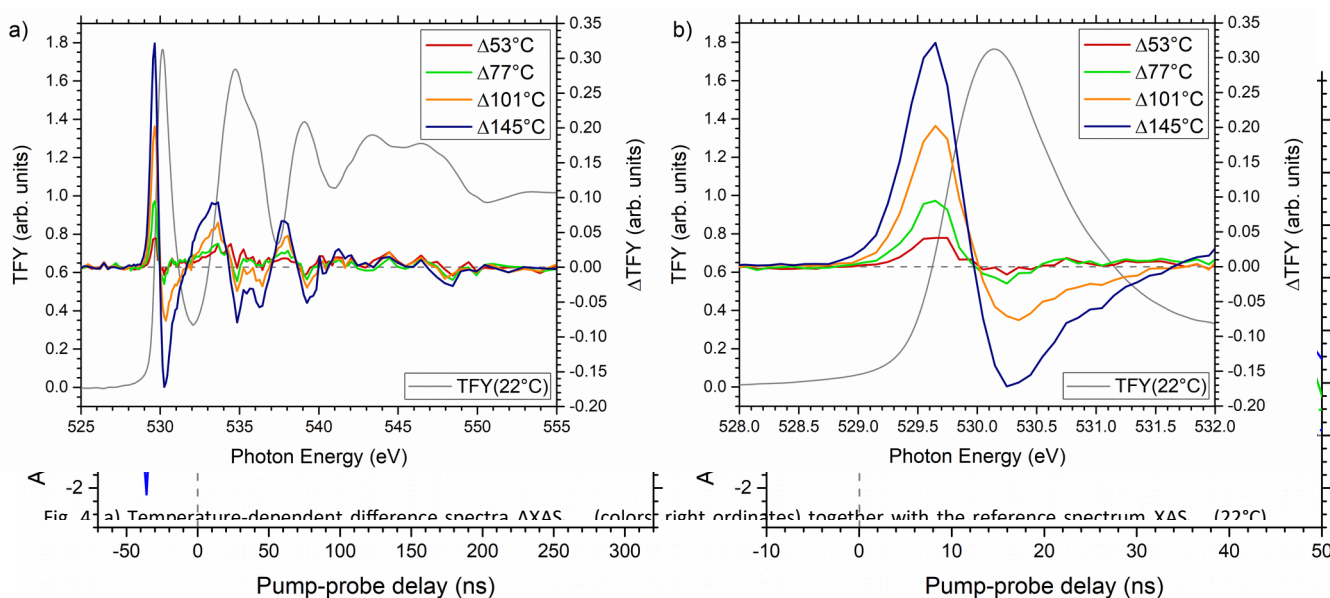

Fig. 4. a) Temperature-dependent difference spectra ΔXAS_{temp} (colors, right ordinates) together with the reference spectrum XAS$_{temp}$ (22°C)

e_g[29]) which is shown in more detail in Fig. 2b. The difference spectra exhibit a new feature emerging at the low-energy side of the static absorption spectrum (gray) with a peak at ~529.4-529.5 eV. Concurrently, signal is depleted near the static peak maximum with a maximum depletion at ~530.3 eV. Within the scatter of the experiment, the ΔtrXAS spectra exhibit an isosbestic point at ~529.9 eV, which separates the signal enhancement and depletion ranges. At first glance, the difference curves resemble differentials of the static XAS spectrum, which would be an indication that they may be described by a simple shift of the XAS spectrum upon photoexcitation, i.e., ΔtrXAS = α* [XAS_{REF}(E-shift) – XAS_{REF}(E)]. However, no combination of the parameters α (fraction of reference spectrum XAS_{REF} that is shifted) and 'shift' (magnitude of shift in X-ray photon energy) can be found that describes the difference spectra reasonably well. This is mostly due to the asymmetry of trXAS signal depletion and emergence, readily apparent in Fig. 2b.

As a first metric to investigate the relaxation dynamics of the photoexcited system, the area underneath the positive peak of the ΔtrXAS spectra in Fig. 2b is plotted as a function of pump-probe delay in Fig. 3. All data sets have been recorded during the same beamtime except for the 355 nm, 2.7 mJ/cm^2 data. In that case, an additional 355 nm, 4.6 mJ/cm^2 scan was performed to ensure it matches the data from the previous experiment and inevitable changes from beamtime to beamtime, such as slight variations of the laser spot size, did not affect the measured signals within the scatter of the data. Each data point in Fig. 3 corresponds to a single pump-probe delay, i.e. specific ALS bunch. The amplitudes and dynamic trends of the new low-energy feature vary for different excitation wavelengths and fluences. For the highest fluences (4.6-4.8 mJ/cm^2), however, they are very similar for both 355 nm and 532 nm excitation. Each of these two data sets display a transient behavior marked by two decay timescales of roughly τ_1=10 ns and τ_2=300 ns. Evidently, the dynamic processes underlying the trXAS signals cannot be characterized by a simple, first-order rate equation. Instead, a more complex description is required that will be derived in

section 4 within the framework of a thermal diffusion model.

Fig. 4 shows the results of the quasi-static, temperature-dependent XAS_{temp} measurements. Fig. 4a shows the room temperature reference spectrum acquired at 22°C in gray (left y-axis). This reference spectrum is subtracted from spectra acquired at elevated temperatures of 53°C, 77°C, 101°C and 145°C to generate the color coded ΔXAS_{temp} difference spectra as indicated in the figure legend. Fig. 4b shows a magnified view of the region near the Cu e_g resonance.[29] The TFY yield axis on the left and ΔTFY axis on the right of each panel correspond to the lowest temperature spectrum (gray) and the higher temperature difference spectra, respectively. A comparison of Fig. 2 and Fig. 4 reveals striking similarities between the temperature-induced difference spectra ΔXAS_{temp} and the photo-induced ΔtrXAS data. For every resonance peak of the XAS spectrum (530.1, ~535 and 539 eV), a positive transient feature appears at its low-energy side (529.65, 533.5 and 537.75 eV) and a depletion feature at its high-energy side (530.3, 535.5 and 539.3 eV). Both the positions and relative heights of these features appear to be very similar in both types of measurements. The second resonance around 535 eV has mainly Cu4s and some Cu3d character[29] and consists of two strongly overlapping peaks. Correspondingly, the ΔXAS_{temp} spectra at higher temperatures exhibit a double depletion feature, whereby the lower energy one (534.8 eV) is likely affected by the positive feature corresponding to the higher energy one (536.2 eV). As in the case of the ΔtrXAS data, the most distinct features appear in the spectral range near the Cu e_g resonance. Interestingly, the ΔXAS_{temp} spectra also exhibit an isosbestic point separating the positive and negative difference signal for all measured temperatures. It is located at ~530.0 eV, very close to the ~529.9 eV value for the ΔtrXAS curves.

4. Data analysis

XAS_{temp} data (Fig. 4) were recorded with significantly better energy resolution than trXAS data and different trXAS data sets have slightly

contains the strongest difference features and   fluence, not the photon energy. In contrast, the

a)

b)
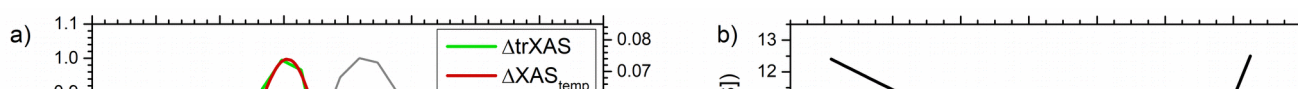
small differences in the energy scaling across more extended NEXAFS ranges make a quantitative comparison across larger energy ranges challenging. Due to the asymmetric peak shape, the convolution changes the peak position as well. Therefore, for each ground state spectrum, two free fit parameters are used to match it to XAS_{ref}, the FWHM of the Gaussian convolution function and a rigid shift of the entire spectrum. In order to prevent artifacts due to small peak height variations, all spectra are scaled to the same Cu e_g peak height of 1. The FWHM, energy shift and scaling values derived using the ground state spectra are then applied to both the ground and corresponding excited state spectra to calculate the ΔtrXAS and ΔXAS_{temp} difference spectra. Fig. 5a shows the

excitation density within the probed volume appears to play a less prominent role, as evidenced by the significant differences between the traces associated with the 355 nm, 2.7 mJ/cm^2 and 532 nm, 4.8 mJ/cm^2 data sets in both Fig. 3 and Fig. 5. In other words, the deposited energy per unit area rather than the number of excitations per unit volume correlates most strongly with the observed transient XAS response, which is a strong indication that thermal effects, rather than electronic excitations, generate the dominant contributions to the ΔtrXAS data.

In order to test this hypothesis, a detailed comparison between the two highest fluence ΔtrXAS data (355 nm, 4.6 mJ/cm^2 and 532 nm,
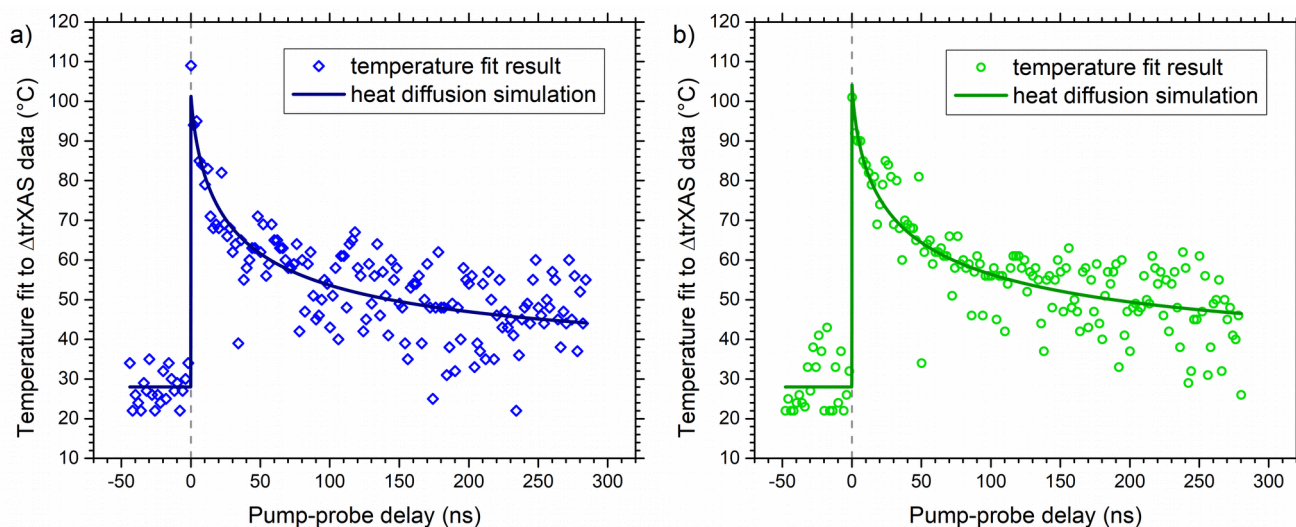
4.8 mJ/cm^2) and the ΔXAS$_{temp}$ data is performed for each pump-probe time delay. The results are used to generate time-dependent sample temperature profiles for the two trXAS measurements, which are interpreted with the aid of a thermal diffusion model. As demonstrated below, the model reproduces the non-trivial dynamic trends indicated in Fig. 3 and provides access to time-dependent surface- and bulk-temperatures as well as the thermal conductivity of the sample.

In a first step, a linear interpolation of the XAS$_{temp}$ spectra measured at 22°C, 53°C, 77°C, 101°C and 145°C is performed in 1°C steps in order estimate the shape of the spectra on a finer temperature grid. Spectra for temperature values >145°C are estimated by a corresponding extrapolation using the 101°C and 145°C data. ΔXAS$_{temp}$ spectra similar to Fig. 4 are generated for all interpolated and extrapolated data beyond 28°C by subtracting the (interpolated) reference spectrum at 28°C from the higher temperature spectra. The slightly elevated reference temperature (compared to the nominal 22°C room temperature) is chosen to account for a slight increase in average temperature during the trXAS measurements that is determined with a thermocouple. The 28°C spectrum is also used to determine the convolution parameters described above to match the energy resolution of the temperature-dependent and time-dependent spectra.

Two different fit procedures are applied to derive the time-dependent temperature profiles of the sample volumes probed by the trXAS measurements. The first method is easier to implement, but partly neglects inhomogeneous temperature effects, which are fully included in the second method. In the following, we discuss the results achieved by both methods in order to illustrate which effects need to be taken into account and which approximations are applicable when modeling thermal effects in trXAS spectra of condensed phase samples.

In the first method, the fit routine determines the temperature T for each time delay Δt, for which the absolute difference between the ΔXAS$_{temp}$(T) and the ΔtrXAS(Δt) spectra (integrated over the energy range of the Cu e$_g$ resonance) is minimal. Fig. 6a shows the result of this fit procedure for

the 532 nm, 4.8 mJ/cm^2 data set at a pump-probe delay of 150 ps. Depicted are the ΔtrXAS(150 ps) spectrum (green) and the best fit (red) corresponding to the curve ΔXAS$_{temp}$(101°C) = XAS$_{temp}$(101°C) – XAS$_{temp}$(28°C). The residual of the fit is shown as a dashed, black curve. Fig. 6b illustrates the convergence of the fit. The black trace is derived by integrating the absolute value of the residual across the energy range 528.25-531.75 eV for all interpolated ΔXAS$_{temp}$(T) spectra. The minimum position corresponds to the best fit shown in Fig. 6a. The best fit quality varies for different time delays and the corresponding residual curve (as shown in Fig. 6b) gets flatter for longer time delays. Nevertheless, the fit always converges to a single temperature to best reproduce the measured ΔtrXAS(Δt) spectrum. Note that the temperature T is the only free parameter of the fit for this method. For any fixed values of T and Δt, the amplitudes of the ΔXAS$_{temp}$(T) and ΔtrXAS(Δt) spectra are determined by normalizing the Cu e$_g$ peak heights of the XAS$_{temp}$(28°C) and the ground state trXAS spectra to 1.

Performing this fit for all pump-probe time-delays

modeled as a one-dimensional diffusion process

leads to the time-dependent temperature estimates displayed in Fig. 7. Fig. 7a shows the results for the 355 nm, 4.6 mJ/cm² data (blue diamonds), Fig. 7b the corresponding results for the 532 nm, 4.8 mJ/cm² data (green circles). Similar to the traces shown in Fig. 3, the dynamic trends are marked by a fast initial decay within 10s of nanoseconds, followed by a much slower relaxation on 100s of nanosecond timescales. The data are interpreted with the aid of a thermal diffusion model represented by the solid curves in Fig. 7.

The model is based on the assumption that a certain amount of thermal energy is deposited by the pump pulse within a near-surface volume and then propagates further into the bulk by thermal diffusion. Heat transport by convection is neglected, since the experiment is conducted at a pressure <5x10⁻⁹ mbar. A simple estimate shows that radiative heat loss is negligible, too. According to the Stefan-Boltzmann law, the total radiated power of a black body at 120°C is ~1.4 kW/m². Using a FWHM laser beam size of roughly 250x250 μm² and a pulse energy of 3 μJ, the fraction of the pulse energy radiated within the first 300 ns is 7x10⁻⁶, which is negligible within the precision of the experiment. Even when allowing for substantially higher temperatures within the first 150 ps before the first probe pulse arrives, the order of magnitude of this estimate would be unaffected. Heat conduction is

along the surface normal, z. For CuO, the optical penetration depths of 21 nm (λ=355 nm) and 125 nm (λ=532 nm)[28,34] as well as the effective X-ray probing depth of 43 nm[35] (see section 2.3) are three to four orders of magnitude smaller than the FWHM of the laser spot (150-250 μm). Furthermore, the diameter of the area probed by the X-ray beam is only about half of the laser spot size. Therefore, the excited and probed sample volumes can be thought of as thin, concentric disks. The characteristic temperature gradients in and around the probed sample volume are thus orders of magnitude larger along the surface normal compared to radial directions parallel to the surface. Consequently, heat transport within the sample may be modeled by diffusion along an insulated cylinder with no lateral heat loss as described by[36,37,38]

$$\frac{dQ}{dt} = -k * A \frac{\delta T(t,z)}{\delta z}. \quad (1)$$

Here, dQ is the amount of thermal energy transferred through a cross-sectional area A per time dt, k is the thermal conductivity and T is the temperature profile as a function of time t and depth z relative to the sample surface. The thermal conductivity is assumed to be constant for simplicity and because slight temperature dependencies would be negligible compared to the overall precision of the analysis presented

here. The temperature distribution at time zero $T(t=0,z)$ is proportional to the derivative of the depth-dependent laser intensity $I_{laser}(z) = exp[-z/\delta_{laser}(\lambda)]$, where δ_{laser} is the laser penetration depth. The amplitude of the resulting exponential function is the initial temperature increase after laser excitation at the surface $\Delta T(t=0,z=0)$. This boundary condition leads to

$$T(t=0,z)=\frac{(1-R)*PE*exp(-z/\delta_{laser})}{2*\rho*A*c(T)*\delta_{laser}}+T_{ref}. \quad (2)$$

where A is the FWHM laser spot size, PE is the laser pulse energy, $R(\lambda)$ the sample reflectivity, $\delta_{laser}(\lambda)$ the 1/e laser penetration depth, ρ the sample density and $c(T)$ its specific heat capacity.[39] The sample equilibrium temperature $T_{ref} = 28°C$ is added to the laser induced temperature jump to convert to an absolute temperature scale $T(t=0,z)$. Using eqn. (2) and the experimental parameters given above, the initial surface temperature estimates are $T(0,0)_{532nm} = 157°C$ and $T(0,0)_{355nm} = 747°C$ for 532 nm (4.8 mJ/cm^2) and 355 nm (4.6 mJ/cm^2) excitation, respectively.

The subsequent thermal diffusion process is modeled numerically by an iterative computer simulation. Based on an initial temperature profile $T(t=0,z)$ according to eqn. (2), it calculates the amount of heat dQ transferred to and from each volume element $A*dz$ within a short time step dt using eqn. (1). The slightly modified thermal energy distribution is used to calculate a new temperature profile $T(t+dt,z)$, which in turn is employed to calculate the depth-dependent heat transfer rates during the next time step and so on. Typical time and depth step sizes are $dt = 10$ ps and $dz = 3$ nm, respectively. Convergence of the simulation is tested by varying these step sizes and ensuring that the results are not affected within the overall precision of the method.

For the first, basic temperature analysis presented in Fig. 7, the effective temperature $T_{eff}(t)$ probed by the X-ray pulse is estimated by multiplying the simulated temperature profile $T(t,z)$ with the probe intensity distribution $I_{X-rays}(z) \sim exp[-z/\delta_{X-rays}]$ and integrating the result over z. Here, δ_{X-rays} is the effective 1/e X-ray escape

depth described in section 2.3. The free parameters varied during the fit are the amplitude of the initial temperature distribution $T(t=0,z=0)$, i.e., the initial surface temperature, and the thermal conductivity k. The best fit results, shown as solid curves in Fig. 7, correspond to thermal conductivities of $k_{355nm} = (0.16\pm0.06)$ Wm^{-1}K^{-1}, $k_{532nm} = (1.3\pm0.5)$ Wm^{-1}K^{-1} and initial surface temperatures of $T(0,0)_{355nm} = (188\pm20)°C$, $T(0,0)_{532nm} = (120\pm11)°C$. While a substantial difference in the initial surface temperatures is to be expected for the two laser colors due to the factor of ~6 difference in absorption depths, the thermal conductivities should ideally be the same within the precision of the method. In order to improve the temperature dynamics estimates and to get a better understanding of factors affecting the precision of the fit results, a second more advanced temperature modeling and dynamics fit procedure is applied.

A key challenge is that the XAS$_{temp}$ spectra are acquired at a single temperature each that is constant throughout the entire sample, while in the trXAS experiments temperatures vary significantly within the probed sample volume. The first, basic method described above hinges on the assumption that an effective temperature T_{eff} can be defined for the probed volume by a weighted average of an extended temperature profile and that the measured ΔtrXAS(t) spectrum emerging from this volume is well represented by the corresponding ΔXAS$_{temp}(T_{eff})$ spectrum measured with a homogeneous temperature T_{eff} across the entire sample. However, the temperature dependence of the ΔXAS$_{temp}$ spectra is nontrivial (see Fig. 4) and, generally, the (weighted) average spectrum

$$\Delta XAS_{temp}^{avg}=\sum_i w_i \Delta XAS_{temp}(T_i)/\sum_j w_j$$ of the probed sample volume does not have to be well approximated by the corresponding difference spectrum ΔXAS$_{temp}(T_{eff})$ measured at the average temperature $$T_{eff}=\sum_i w_i(T_i)/\sum_j w_j.$$ The quality of the approximation is expected to depend strongly on the range of temperatures within the probed volume. For the 532 nm data, the optical penetration depth (125 nm) is significantly larger than the X-ray probing depth (43 nm), leading to a relatively homogeneous temperature

distribution within the probed sample volume and the approximation is expected to hold fairly well. In contrast, for 355 nm excitation, the penetration depth (21 nm) is much smaller than the X-ray probing depth, resulting in a strongly inhomogeneous temperature distribution within

$$\Delta trXAS_i(E,t_N) = \sum_z I_{X-rays}(z) \Delta XAS_{temp}(E,T_N(z)) / \sum_{z'} I_x$$

. (3)

During the fit procedure, the values of k and $T(0,0)$ are varied such that the sum of *all*

a)

b)
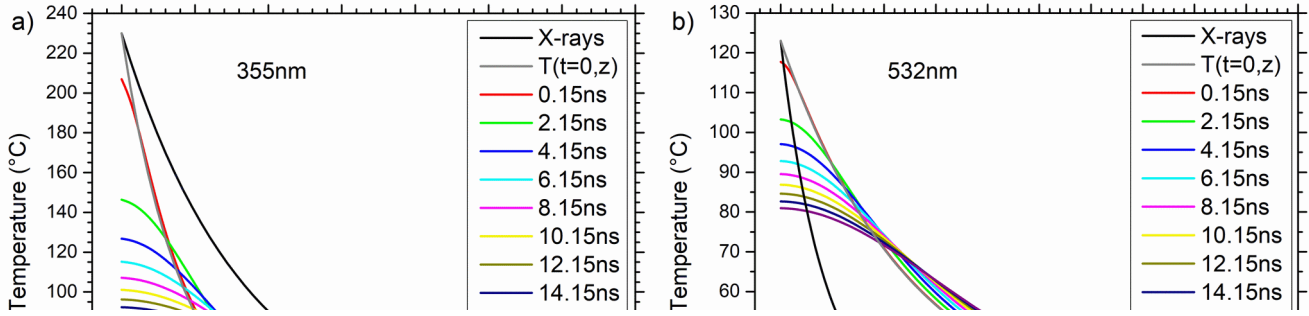
the probed volume, at least for short pump-probe delays. In this case, the approximation is expected to break down.

In order to avoid potential shortcomings of the effective "homogeneous" temperature approach, a modified "inhomogeneous" fit procedure is applied that explicitly takes into account both the time- and depth-dependent temperature profiles as well as the complex correlation between local temperatures and corresponding ΔXAS_{temp} profiles. Starting with a thermal conductivity value k and an initial surface temperature $T(0,0)$, the 2D matrix $T(t,z)$ of a time- and depth-dependent temperature profile is calculated using the numerical model based on eqn. (1). This provides, in particular, a temperature distribution $T_N(z)$ at the time of arrival of each probe pulse N, i.e., $T_N(z)=T(t_N=t(bunch \ N), z)$. The simulated spectrum $\Delta trXAS_{sim}(E, t_N)$ for each bunch N is then calculated as the weighted average of the $\Delta XAS_{temp}(E, T_N(z))$ spectra using the X-ray intensity distribution $I_{X-rays}(z) \sim exp[-z/\delta_{X-rays}]$ as the weight function:

residuals

$$R_{total} = \sum_N R_N = \sum_N \sum_E |\Delta trXAS_i(E,t_N) - \Delta trXAS(E,t_N)|$$

for all energies E within the range 528.25 - 531.75 eV and for all times t_N is minimized. This inhomogeneous fit procedure leads to best fit values of $k_{355nm} = 0.29^{+0.11}_{-0.07}$ Wm^{-1}K^{-1}, $k_{532nm} =$ (1.3±0.4) Wm^{-1}K^{-1} for the heat conductivities and $T(0,0)_{355nm} =$ (230±28)°C, $T(0,0)_{532nm} =$ (123±10)°C for the initial surface temperatures at the two excitation wavelengths. Uncertainties correspond to one sigma standard deviations computed from the fit residuals according to eqn. 12 in reference 40. As expected, the values for 532 nm are very similar to the results derived with the homogeneous, effective temperature fit model, while the values for 355 nm differ considerably.

Fig. 8 shows a comparison of the results from the two modeling procedures for both excitation wavelengths. Gray circles are the result of the homogeneous, single effective temperature fits

a)

b)
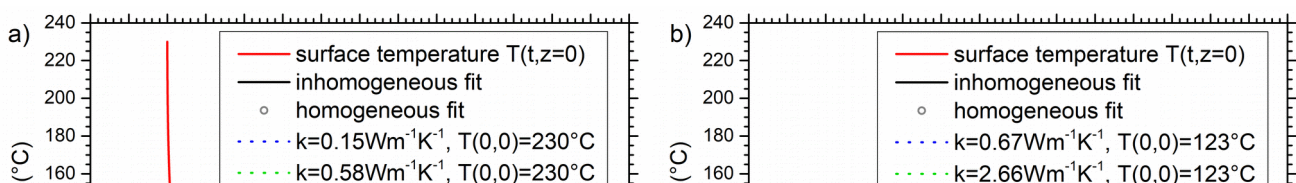
surface temperatures $T(0,0)$ constant. The red solid lines indicate the time-dependence of the surface temperatures, $T(t,0)$, from the global fit model. The most significant difference between the different models is the much higher initial surface temperature for 355 nm in the global fit model. The large differences between the depth-averaged temperatures (gray, black) and the reconstructed surface temperatures (red) for the 355 nm data are rooted in the mismatch between the short UV absorption depth of CuO and the comparably larger X-ray escape depth described above. This mismatch is illustrated in more detail in Fig. 9a, which shows the temperature distribution at time zero (gray line) and for the first nine probe pulses (colored lines) after 355 nm excitation, reconstructed with the global fit model. Fig. 9b shows the corresponding trends for the 532 nm data. For comparison, the X-ray escape profile, offset by the sample equilibrium temperature and scaled to the initial surface temperature, is overlaid as a solid black line. Note the different ranges of z-values in Fig. 9a and 9b. As expected from the different optical penetration depths, the temperature profiles have much higher gradients and spread across a larger range of values for the 355 nm compared to the 532 nm experiment. We note that the appearance of significantly higher surface temperatures in the 355 nm compared to the 532 nm experiment is independently corroborated by a more efficient conversion of CuO to Cu_2O upon UV excitation of the sample compared to the visible excitation. This leads to the emergence of an additional signal in the CuO XAS spectrum at the location of the ~532 eV white line of the Cu_2O spectrum (see Fig. 1a), which needs to be suppressed by a faster raster scan speed in the 355 nm experiment compared to the 532 nm experiment and by scanning every sample spot only once. Thus, the striking similarities between the observed temperature dynamics for 355 nm and 532 nm excitation displayed in Fig. 7 and 8 to some degree conceal

spectra of CuO beyond ~100 ps pump-probe delay are dominated by thermal effects. This observation is in agreement with the results of Hayes et al.[7] and Lin et al.[8] for super-bandgap excited α-Fe_2O_3 and PbI_2, respectively. Lin et al. excited ~70 nm thick polycrystalline films of PbI_2 (deposited on 50 nm thick silicon nitride) with 400 nm radiation and probed the induced dynamics with femtosecond time-resolved XUV absorption at the I 4d level (~50 eV[8]). They found good agreement between the photoinduced XUV absorption change after 40 – 100 ps and a temperature-dependent absorption change induced by heating the sample from 20°C to 120°C. A complementary ultrafast electron diffraction experiment by the same group corroborated the finding that temperature effects start to dominate the pump-probe difference spectra after ~4 ps.[8] Hayes et al. performed oxygen and iron K-edge trXAS measurements on 20 nm thick films of hematite (α-Fe_2O_3, deposited on 100 nm thick silicon nitride) excited with 400 nm and 351 nm pulses, respectively.[7] The Fe K-edge ΔtrXAS spectrum at 100 ps pump-probe delay is well reproduced by a ΔXAS_{temp} spectrum generated by subtracting steady-state XAS spectra recorded at ~30°C from one acquired at ~230°C. Corresponding theoretical modeling of the spectra using multiple scattering calculations confirmed that the dominant effects in the ΔtrXAS spectrum are indeed due to thermal effects with contributions from both thermal disorder and lattice distortions.[7]

The study presented here reproduces a predominance of lattice temperature induced effects in picosecond trXAS for another transition metal oxide semiconductor. In addition, it provides further insight into the temporal evolution of lattice temperature profiles after laser excitation on an absolute temperature scale with a temporal sensitivity and a spatial selectivity on the order of 10s of picoseconds

and 10s of nanometers, respectively. The results presented in Fig. 7 and 8 indicate that the heat transport dynamics may be approximated by a one-dimensional diffusion model as previously employed in picosecond time-resolved electron diffraction studies of laser-heated metal surfaces.[36] However, the comparison of the trXAS results for 355 nm and 532 nm excitation also reveals that a quantitative interpretation of the underlying physics requires detailed understanding and modeling of the relation between the temperature distribution within the sample and the resulting X-ray spectroscopic signatures. In order to understand and predict thermal effects in time-dependent X-ray absorption spectra, it should be ensured that the X-ray probing depth is small compared to the penetration depth of the optical excitation. Otherwise, signal contributions from regions with significantly different temperatures need to be disentangled. This effect is documented by the significant fit-model dependence of both the reconstructed temperature profiles as well as the thermal conductivity k in the 355 nm experiment. In contrast, the corresponding results for the 532 nm measurements are largely model-independent.

Additional evidence that the 532 nm experiment is better understood on a quantitative level is provided by a comparison of the fit results with surface temperature predictions based on eqn. (2). The calculated surface temperature after absorption of a 532 nm pump pulse is $T(0,0)_{532nm}(calc) = 157°C$, which agrees reasonably well with the outcome of the global fit $T(0,0)_{532nm}(fit) = 123°C$. In contrast, the corresponding values for 355 nm excitation are $T(0,0)_{355nm}(calc) = 747°C$, $T(0,0)_{355nm}(fit) = 230°C$, i.e., the calculated and reconstructed temperature jumps differ by a factor of ~3.6. The reason for this large discrepancy is currently unknown. One contributing factor may be that, despite our best efforts, the convolution methods described in section 4 could provide an inaccurate modeling of the ΔtrXAS response if the sampled region exhibits a steep-gradient temperature distribution. Another potential issue is that the ΔXAS_{temp} spectra for temperatures above 145°C have been estimated based on a linear extrapolation of the measurements at 101°C and 145°C, which is most likely increasingly inaccurate with increasing temperatures. Interestingly, however, Hayes et al. also observed a significant discrepancy between the estimated temperature rise in their

hematite sample based on the absorbed photon energy (~470°C) and the steady-state temperature rise needed to reproduce the photon-induced change in X-ray absorption (200°C).[7] In this case, temperature gradients should not play a major role due to the small sample thickness of only 20 nm. Note that in both cases, the hematite experiment using 351 nm excitation and the CuO experiment at 355 nm excitation, the temperature rise estimated by a complete conversion of the absorbed laser pulse energy into heat is much larger than the measured temperature increase based on a comparison to steady-state temperature-dependent ΔXAS_{temp} spectra. A possible contributor to such an effect could be the appearance of radiative relaxation channels that would effectively make some of the deposited photon energy unavailable for lattice heating.

Given the challenges associated with the quantitative analysis of the 355 nm experiment, we restrict a more detailed discussion of the fit results to the 532 nm measurement. The good agreement between the observed and reconstructed temperature dynamics illustrated in Fig. 7b, between the absolute temperature values derived from the absorbed laser pulse energy and the dynamics fit, as well as the model-independence of the fit results for 532 nm excitation suggest that heat transport within the CuO sample is well represented by a thermal diffusion constant $k = (1.3\pm0.4)$ Wm^{-1}K^{-1}. Literature values for the thermal conductivity of CuO vary across almost two orders of magnitude from 1.013 Wm^{-1}K^{-1} [24] to 18 Wm^{-1}K^{-1} [25], 33 Wm^{-1}K^{-1} [41] and 78 Wm^{-1}K^{-1}.[42] We note, however, that an extensive literature search did not yield any original reference that would describe the experiments used to derive any of these values. Thus, it is not entirely clear whether the large variance is primarily the result of different sample preparation techniques or of uncertainties in the measurements. Notably, however, the smallest value, reported by Samsonov[24] is the only one for which the sample form is indicated as powder. Given that this value is remarkably close to the one derived here and that all other literature values are more than an order of magnitude larger, it appears that the thermal conductivity of the CuO film prepared in this study most closely resembles that of a CuO powder.

At first glance, this result may be surprising as the sample is prepared by annealing a solid sheet of copper. Note,

however, that the CuO sample consists of a relatively thin film at the Cu surface and the oxidation process is likely accompanied by significant changes in the surface morphology. Gong et al. annealed sputtering deposited thin films of copper in air at temperatures between 200°C and 400°C and studied the resulting surfaces using X-ray diffraction (XRD), Raman spectroscopy, and atomic force microscopy (AFM).[26] They concluded that, below 300°C, Cu is oxidized to Cu_2O and, upon further temperature increase ≥300°C, CuO is formed. In particular, the AFM images reveal substantial surface morphology variations during the phase transitions. During the Cu_2O formation, the surface roughness increases from ~10s to ~100s of nanometer while grains of Cu_2O form and coalesce to typical grain sizes of ~150 nm. At 400°C, CuO forms in lamellar secondary grains with a thickness of ~5 nm, which are distributed within the larger Cu_2O grains. Based on these observations, it is conceivable that the CuO film prepared here by heating of a Cu surface in air to 500°C is also marked by a nano-structured morphology rather than a crystalline bulk structure. In this case, the thermal conductivity of the film may be expected to lie closer to the value for a CuO powder than a crystalline bulk sample. Further characterization of the CuO film using alternative techniques may provide additional insight in this regard.

6. Conclusion and outlook

Photoinduced changes in the oxygen K-edge X-ray absorption spectrum of a thin film of CuO have been studied by picosecond time-resolved XAS and complementary steady-state temperature-dependent XAS. The results show that for pump-probe delays ≥150 ps, the trXAS spectra are dominated by lattice temperature induced effects for both 355 nm and 532 nm excitation. The laser-induced heating and subsequent sample cooling dynamics at pump laser fluences of ~5 mJ/cm^2 are well described by a one-dimensional thermal diffusion model that explicitly takes into account the depth-dependence of both the optical excitation and the X-ray probing. A comparison of the measurements with different pump laser wavelengths shows that a detailed modeling of these depth-dependent profiles is crucial for a quantitative understanding of the thermal dynamics in terms of the material properties. Vice-versa, predicting the impact of thermal

excitations on future trXAS studies will require a correspondingly well-developed understanding of the sample properties and nanoscale intensity profiles of pump- and probe-pulse intensities. The thermal conductivity of the CuO sample used in this study, $k = (1.3 \pm 0.4)$ Wm^{-1}K^{-1}, is in good agreement with the literature value for CuO powder, $k_{powder} = 1.013$ Wm^{-1}K^{-1},[24] and approximately an order of magnitude smaller than the smallest literature value for bulk CuO, $k_{bulk} = 18$ Wm^{-1}K^{-1}.[25] This underlines the importance of proper sample characterization during the planning phase of a trXAS experiment. A prediction of, for example, how fast thermal excitations in the CuO film may be removed between pump-pulses of a high repetition-rate trXAS experiment would lead to a far too optimistic estimate if it were based on the bulk properties of cupric oxide. Note, however, that a predictive understanding of thermal dynamics and their spectral fingerprints and is not only important to mitigate sample damage and unwanted signal contributions but also to perform experiments where photoinduced thermal excitations are the actual trigger for the dynamics under investigation.[5] The results presented here demonstrate that a quantitative modeling of thermal effects in trXAS spectra is possible but also that it requires great dedication to detail regarding the material properties and experimental conditions of the pump-probe experiment to make quantitatively accurate predictions.

7. Conflicts of interest

There are no conflicts to declare.

8. Acknowledgments

9. References

1   M. L. Grünbein, J. Bielecki, A. Gorel, M. Stricker, R. Bean, M. Cammarata, K. Dörner, L. Fröhlich, E. Hartmann, S. Hauf, M. Hilpert, Y. Kim, M. Kloos, R. Letrun, M. Messerschmidt, G. Mills, G. Nass Kovacs, M. Ramilli, C. M. Roome, T. Sato, M. Scholz, M. Sliwa, J. Sztuk-Dambietz, M. Weik, B. Weinhausen, N. Al-Qudami, D. Boukhelef, S. Brockhauser, W. Ehsan, M. Emons, S. Esenov, H. Fangohr, A. Kaukher, T. Kluyver, M. Lederer, L. Maia, M. Manetti, T. Michelat, A. Münnich, F. Pallas, G. Palmer, G. Previtali, N. Raab, A. Silenzi, J. Szuba, S. Venkatesan, K. Wrona, J. Zhu, R. B. Doak, R. L. Shoeman, L. Foucar, J.-P. Colletier, A. P. Mancuso, T. R. M. Barends, C. A. Stan and I. Schlichting, *Nature Communications*, 2018, **9**, 3487.

2   R. W. Schoenlein et al., LCLS-II Science Opportunities, Report SLAC-R-1053 (SLAC National Accelerator Laboratory, Menlo Park CA), https://portal.slac.stanford.edu/sites/lcls_public/Lists/Publications/DispForm.aspx?ID=1004&ContentTypeId=0x0100D2D2C16F06384A44A845B10E6FC226F600DC7CB9184F2FB34484887A99919A7390, (accessed 1 December 2018).

3   S. M. Teichmann, F. Silva, S. L. Cousin, M. Hemmer and J. Biegert, *Nature Communications*, 2016, **7**, 11493.

4   D. Popmintchev, B. R. Galloway, M.-C. Chen, F. Dollar, C. A. Mancuso, A. Hankla, L. Miaja-Avila, G. O'Neil, J. M. Shaw, G. Fan, S. Ališauskas, G. Andriukaitis, T. Balčiunas, O. D. Mücke, A. Pugzlys, A. Baltuška, H. C. Kapteyn, T. Popmintchev and M. M. Murnane, *Physical Review Letters*, 2018, **120**, 093002.

5   H. Öström, H. Öberg, H. Xin, J. LaRue, M. Beye, M. Dell, J. Gladh, M. L. Ng, J. A. Sellberg, S. Kaya, G. Mercurio, D. Nordlund, M. Hantschmann, F. Hieke, D. Kühn, W. F. Schlotter, G. L. Dakovski, J. J. Turner, M. P. Minitti, A. Mitra, S. P. Moeller, A. Föhlisch, M. Wolf, W. Wurth, M. Persson, J. K. Nørskov, F. Abild-Pedersen, H. Ogasawara, L. G. M. Pettersson and A. Nilsson, *Science*, 2015, **347**, 978–982.

6   M. Schultze, K. Ramasesha, C. D. Pemmaraju, S. A. Sato, D. Whitmore, A. Gandman, J. S. Prell, L. J. Borja, D. Prendergast, K. Yabana, D. M. Neumark and S. R. Leone, *Science*, 2014, **346**, 1348–1352.

7   D. Hayes, R. G. Hadt, J. D. Emery, A. A. Cordones, A. B. F. Martinson, M. L. Shelby, K. A. Fransted, P. D. Dahlberg, J. Hong, X. Zhang, Q. Kong, R. W. Schoenlein and L. X. Chen, *Energy & Environmental Science*, 2016, **9**, 3754–3769.

8   M.-F. Lin, M. A. Verkamp, J. Leveillee, E. S. Ryland, K. Benke, K. Zhang, C. Weninger, X. Shen, R. Li, D. Fritz, U. Bergmann, X. Wang, A. Schleife and J. Vura-Weis, *The Journal of Physical Chemistry C*, 2017, **121**, 27886–27893.

9   S. Harish, J. Archana, M. Sabarinathan, M. Navaneethan, K. D. Nisha, S. Ponnusamy, C. Muthamizhchelvan, H. Ikeda, D. K. Aswal and Y. Hayakawa, *Applied Surface Science*, 2017, **418**, 103–112.

10 R. Saravanan, S. Karthikeyan, V. K. Gupta, G. Sekaran, V. Narayanan and A. Stephen, *Materials Science and Engineering: C*, 2013, **33**, 91–98.

11 S. Xu, A. J. Du, J. Liu, J. Ng and D. D. Sun, *International Journal of Hydrogen Energy*, 2011, **36**, 6560–6568.

12 J. Yu, Y. Hai and M. Jaroniec, *Journal of Colloid and Interface Science*, 2011, **357**, 223–228.

13 J. Bandara, C. P. K. Udawatta and C. S. K. Rajapakse, *Photochemical & Photobiological Sciences*, 2005, **4**, 857.

14 W. Zhang, G. Ma, H. Gu, Z. Yang and H. Cheng, *Journal of Power Sources*, 2015, **273**, 561–565.

15 S. Neppl, J. Mahl, A. S. Tremsin, B. Rude, R. Qiao, W. Yang, J. Guo and O. Gessner, *Faraday Discussions*, 2016, **194**, 659–682.

16 N. Serin, T. Serin, Ş. Horzum and Y. Çelik, *Semiconductor Science and Technology*, 2005, **20**, 398–401.

17 B. Balamurugan and B. R. Mehta, *Thin Solid Films*, 2001, **396**, 90–96.

18 F. Marabelli, G. B. Parravicini and F. Salghetti-Drioli, *Physical Review B*, 1995, **52**, 1433–1436.

19 M. T. . Nair, L. Guerrero, O. L. Arenas and P. . Nair, *Applied Surface Science*, 1999, **150**, 143–151.

20 S. C. Ray, *Solar Energy Materials*, 2001, **68**, 307–312.

21 C. E. Ekuma, V. I. Anisimov, J. Moreno and M. Jarrell, *The European Physical Journal B*, 2014, **87**, 23.

22 M. Dahrul, H. Alatas and Irzaman, *Procedia Environmental Sciences*, 2016, **33**, 661–667.

23 J. F. Pierson, A. Thobor-Keck and A. Billard, *Applied Surface Science*, 2003, **210**, 359–367.

24 G. V. Samsonov, *The Oxide Handbook*, IFI/Plenum, New York, 1973.

25 A. L. Edwards, *A Compilation Of Thermal Property Data For Computer Heat-Conduction Calculations*, Report No. UCRL-50589, 1969.

26 Y. S. Gong, C. Lee and C. K. Yang, *Journal of Applied Physics*, 1995, **77**, 5422–5425.

27 L. De Los Santos Valladares, D. H. Salinas, A. B. Dominguez, D. A. Najarro, S. I. Khondaker, T. Mitrelias, C. H. W. Barnes, J. A. Aguiar and Y. Majima, *Thin Solid Films*, 2012, **520**, 6368–6374.

28 D. Tahir and S. Tougaard, *Journal of Physics: Condensed Matter*, 2012, **24**, 175002.

29 P. Jiang, D. Prendergast, F. Borondics, S. Porsgaard, L. Giovanetti, E. Pach, J. Newberg, H. Bluhm, F. Besenbacher and M. Salmeron, *The Journal of Chemical Physics*, 2013, **138**, 024704.

30 S. Eisebitt, T. Böske, J.-E. Rubensson and W. Eberhardt, *Physical Review B*, 1993, **47**, 14103–14109.

31 A. S. Tremsin, O. H. Siegmund, J. S. Hull, J. V. Vallerga, J. B. McPhate, J. Soderstrom, J.-W. Chiou, J. Guo and Z. Hussain, *IEEE Nuclear Science Symposium Conference Record*, 2006, **2**, 735–739.

32 S. Poulston, P. M. Parlett, P. Stone and M. Bowker, *Surface and Interface Analysis: An International Journal devoted to the development and application of techniques for the analysis of surfaces, interfaces and thin films*, 1996, **24**, 811–820.

33 M. Heinemann, B. Eifert and C. Heiliger, *Physical Review B*, 2013, **87**, 115111.

34 W. K. C. Yung, B. Sun, Z. Meng, J. Huang, Y. Jin, H. S. Choy, Z. Cai, G. Li, C. L. Ho, J. Yang and W. Y. Wong, *Scientific Reports*, 2016, **6**, 39584.

35 CuO - X-ray attenuation length, http://henke.lbl.gov/optical_constants/atten2.html, (accessed 28 November 2018).

36 H. E. Elsayed-Ali and J. W. Herman, *Applied Physics Letters*, 1990, **57**, 1508–1510.

37 J. H. Bechtel, *Journal of Applied Physics*, 1975, **46**, 1585–1593.

38 J. Crank, *The Mathematics of Diffusion*, Oxford University Press, Oxford, England, second edition, 1975.

39 copper oxide - National Insitute for Standards and Technology, https://webbook.nist.gov/cgi/cbook.cgi?ID=C1317380&Type=JANAFS&Table=on, (accessed 28 November 2018).

40 P. J. Cumpson and M. P. Seah, *Surface and Interface Analysis*, 1992, **18**, 345–360.

41 M. Liu, M. Lin and C. Wang, *Nanoscale Research Letters*, 2011, **6**, 297.

42 D. Anandan and K. S. Rajan, *Asian J. Sci. Res.*, 2012, **5**, 218–227.